

SCIENTIFIC REPORTS

OPEN

Crystal structure, equation of state, and elasticity of phase H (MgSiO_4H_2) at Earth's lower mantle pressures

Jun Tsuchiya^{1,2} & Mainak Mookherjee^{3,4}

Received: 23 March 2015

Accepted: 28 September 2015

Published: 23 October 2015

Dense hydrous magnesium silicate (DHMS) phases play a crucial role in transporting water in to the Earth's interior. A newly discovered DHMS, phase H (MgSiO_4H_2), is stable at Earth's lower mantle, i.e., at pressures greater than 30 GPa. Here we report the crystal structure and elasticity of phase H and its evolution upon compression. Using first principles simulations, we have explored the relative energetics of the candidate crystal structures with ordered and disordered configurations of magnesium and silicon atoms in the octahedral sites. At conditions relevant to Earth's lower mantle, it is likely that phase H is able to incorporate a significant amount of aluminum, which may enhance the thermodynamic stability of phase H. The sound wave velocities of phase H are ~2–4% smaller than those of isostructural δ -AlOOH. The shear wave impedance contrast due to the transformation of phase D to a mixture of phase H and stishovite at pressures relevant to the upper part of the lower mantle could partly explain the geophysical observations. The calculated elastic wave velocities and anisotropies indicate that phase H can be a source of significant seismic anisotropy in the lower mantle.

Water plays a crucial role in sustaining geological activity of our planet by affecting melting relationships¹ in the solid Earth and also influencing its rheology^{2–4}. Hence, considerable research has been conducted to understand the transport of water into the Earth's interior⁵ and the thermodynamic stability^{6,7} and the elasticity⁸ of hydrous mineral phases. It is known that ocean water interacts with the underlying oceanic crusts and the exposed peridotite along related bending faults in the oceanic crusts^{9,10} and forms hydrous minerals such as serpentine. As the oceanic plates subduct, the hydrous phases, including serpentine, are dragged along with the plate, and upon compression serpentine transforms to DHMS phases^{11,12}. A series of high-pressure experimental studies have been performed to understand the thermodynamic stability of DHMS phases. These experiments demonstrated that phase D ($\text{MgSi}_2\text{O}_6\text{H}_2$) was thermodynamically stable at the Earth's lower mantle conditions and did not show any further transformation to any other denser hydrous phase^{13,14}, whereas there have been suggestions that phase D might decompose or transform above 44 GPa^{15,16}.

Recently, first principles simulations predicted a new DHMS phase, phase H (MgSiO_4H_2)¹⁷, to be stable at pressures greater than the stability field of phase D. First principles simulations predicted that upon compression (~40 GPa) phase D should decompose to phase H and a high-pressure polymorph of silica (SiO_2), stishovite. This prediction was later confirmed by high-pressure experiments using *in situ* X-ray diffraction measurements with the sintered diamond multi-anvil apparatus¹⁸. Phase H has a crystal

¹Geodynamics Research Center, Ehime University, 2–5 Bunkyo-cho, Matsuyama, Ehime 790–8577 JAPAN.

²Earth-Life Science Institute Ehime Satellite, 2–5 Bunkyo-cho, Matsuyama, Ehime 790–8577 JAPAN. ³Earth and Atmospheric Sciences, Cornell University, 2122 Snee Hall, Ithaca, NY 14853 USA. ⁴Earth, Ocean, and Atmospheric Sciences, Florida State University, Tallahassee, FL 32306 USA. Correspondence and requests for materials should be addressed to J.T. (email: junt@ehime-u.ac.jp)

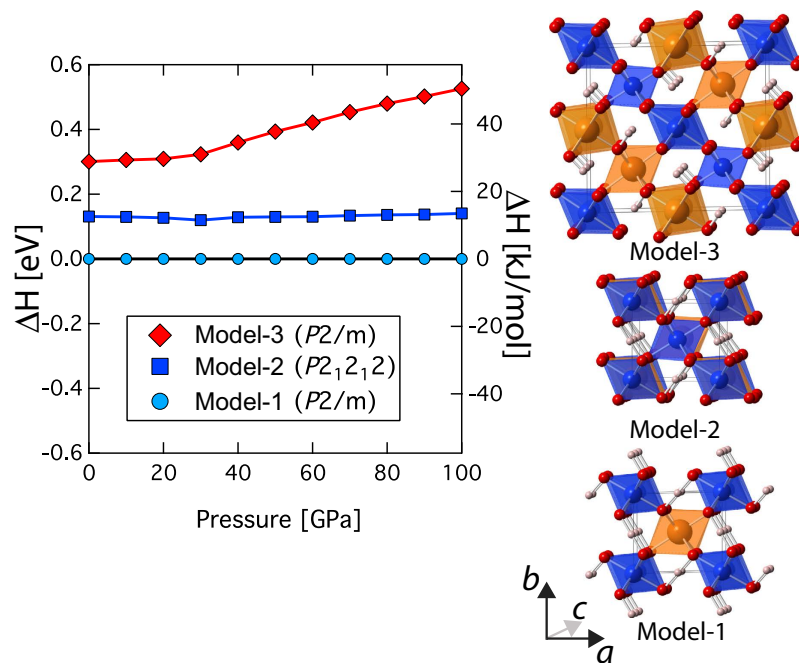


Figure 1. Energetics of order-disorder in phase H. Left panel shows the plot of enthalpy as a function of pressure for model-1, model-2, and model-3. In the right panel, the optimized zero pressure crystal structures for model-1, model-2, and model-3 are shown.

structure consisting of magnesium (Mg) and silicon (Si) atoms in an octahedral coordination and is similar to the crystal structure of δ -AlOOH^{17,18} where aluminum (Al) atoms occur in octahedral sites. Owing to the possibility of the configurational disorder of the Mg and Si atoms in the octahedral sites, the space group symmetry of phase H was subsequently refined using the single-crystal X-ray diffraction method¹⁹.

Despite being an important candidate for transporting water into the deep Earth, the crystal structure and elasticity of phase H at high pressures are unknown. In this study, using first principles simulations, we report the crystal structure of phase H including the effect of ordering and disordering of Mg and Si atoms in the octahedral sites. We also determine the equation of state, full-elastic constant tensor, and the elastic anisotropy of phase H at pressures relevant to Earth's lower mantle pressure conditions.

Results

Energetics calculations, considering the effects of Mg and Si order-disorder reveal that the model-1 with $P2/m$ space group symmetry has the lowest enthalpy across all pressures relevant for Earth's interior (Fig. 1). Model-2 with space group symmetry of $P2_12_12$ show slightly greater enthalpy (~ 0.13 eV/Z, where Z = formula unit in the unit-cell) than model-1. The pressure-volume results for phase H are well described by the finite strain formulation of Birch-Murnaghan²⁰ (Fig. 2) with a zero pressure bulk modulus K_0 of $147.5 (\pm 6.8)$ GPa, the pressure derivative of the zero pressure bulk modulus K_0' of $4.9 (\pm 0.2)$, and a zero pressure unit-cell volume V_0 of $58.9 (\pm 0.2)$ Å³. The predicted lattice parameters are in good agreement with the experimental results^{18,19} (Fig. 2, Table 1, Supplementary Table 1). The predicted monoclinic distortion in γ , i.e., deviation from orthogonal angle (90°) is minor and remains within $\pm 3^\circ$ at all pressures explored in this study. Upon compression, the hydroxyl bond (r_{O-H}) increases in its length and the distance between the pair of oxygen atoms ($r_{O...O}$) decreases, ultimately forming a symmetric hydrogen bond, i.e., $r_{O-H} = (1/2)r_{O...O}$ at ~ 30 GPa. The hydrogen bond symmetrization has also been predicted for an isostructural dense hydrous phase such as δ -AlOOH phase using first principles simulations^{21,22} and later confirmed by experiments^{23,24}.

The components of the full elastic constant tensor of phase H increase with pressure (Table 2, Fig. 3). The principal elastic constants C_{11} and C_{22} , the off-diagonal elastic constants C_{23} , C_{16} , and C_{26} , and the shear elastic constant C_{66} show anomalous increase at ~ 30 GPa (Fig. 3). The pressure dependent anomalous behavior in the elastic constant is predicted for both the ordered (model-1) and disordered (model-2) phase H structures (Supplementary Table 2). The likely cause for such pressure dependent anomalous behavior in elasticity is the symmetrization of hydrogen bonds. Similar anomalous behavior in elasticity for the isostructural δ -AlOOH phase have also been explained by hydrogen bond symmetrization²¹. In the present study, although, the anomalous behavior occurs at ~ 30 GPa, it is possible that the quantum and thermal vibrational effects may affect the pressure where hydrogen bond symmetrizes and also the

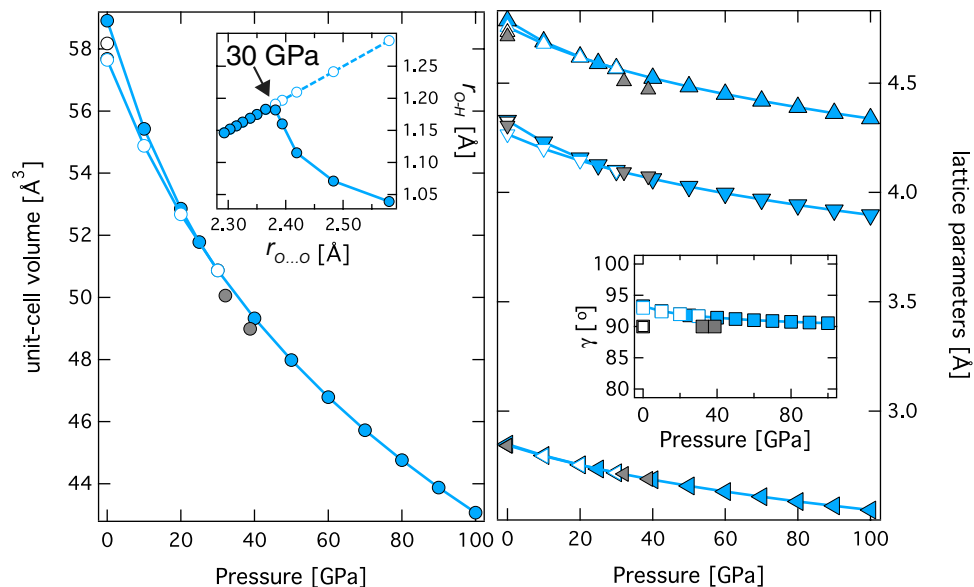


Figure 2. Pressure dependence of unit-cell volume and lattice parameters. The left panel shows the plot of unit-cell volume as a function of pressure for phase H with ordered Mg and Si atoms (model-1) (light blue filled symbol). Also, shown are the metastable extensions of unit-cell volume for the symmetric hydrogen bonded structure (light blue open symbols). Inset shows the plot of r_{O-H} as a function of $r_{O...O}$, at around 30 GPa, r_{O-H} becomes (1/2) of $r_{O...O}$, i.e., hydrogen bond symmetrizes. The right panel shows the plot of the a -, b -, and c -axes as a function of pressure. Inset shows the plot of γ as a function of pressure. For comparison, the experimental results are also plotted (open symbols)¹⁸ and (grey filled symbols)¹⁹.

P (GPa)	ρ (g/cm ³)	a (Å)	b (Å)	c (Å)	γ (°)	r_{O-H} (Å)	$r_{O...O}$ (Å)	MgO ₆ (Å ³)	SiO ₆ (Å ³)
0	3.338	4.786	4.328	2.848	93.3	1.039	2.580	12.1	8.1
10	3.547	4.689	4.230	2.797	92.5	1.071	2.483	11.3	7.8
20	3.720	4.620	4.157	2.754	92.0	1.115	2.419	10.7	7.5
25	3.797	4.590	4.126	2.735	91.8	1.160	2.394	10.4	7.4
30	3.865	4.567	4.100	2.718	91.7	1.182	2.382	10.2	7.3
40	3.986	4.523	4.062	2.686	91.4	1.183	2.365	9.8	7.2
50	4.098	4.484	4.027	2.658	91.2	1.175	2.350	9.5	7.0
60	4.202	4.449	3.996	2.632	91.0	1.169	2.338	9.2	6.9
70	4.300	4.418	3.968	2.609	90.9	1.163	2.325	9.0	6.7
80	4.393	4.389	3.943	2.587	90.7	1.157	2.314	8.7	6.6
90	4.481	4.362	3.919	2.567	90.6	1.152	2.303	8.5	6.5
100	4.565	4.338	3.897	2.548	90.5	1.146	2.293	8.4	6.4

Table 1. Cell parameters, hydroxyl (r_{O-H}) bond distances, oxygen-oxygen ($r_{O...O}$) bond distances, and polyhedral volumes of phase H (model-1) as a function of pressure.

onset of anomalous behaviors²⁵. At pressures beyond the hydrogen bond symmetrization, all the elastic constants stiffen steadily upon compression without further pressure dependent anomalous behavior. It is interesting to note that the predicted C_{33} is smaller than C_{11} and C_{22} at pressures beyond the hydrogen bond symmetrization (i.e., 30–100 GPa), though the crystal structure of phase H consists of edge shearing SiO₆ and MgO₆ octahedral units which are densely packed along the c -axis. Since the Mg-O and Si-O bonds are not directly aligned along the c -axis, compression along the c -axis can be achieved relatively easily by the alteration of the Si-O-Si and Mg-O-Mg angles. The elastic constants C_{11} and C_{22} of the model-2 structure are similar to those of model-1, whereas C_{33} of model-2 is about 5% smaller than that of model-1 (Supplementary Table 2). The model-2 type phase H is likely to be mechanically unstable at low pressure conditions since the shear elastic constant, C_{55} of <0 at ~ 0 GPa.

P (GPa)	ρ (g/cm ³)	C_{11} (GPa)	C_{12} (GPa)	C_{13} (GPa)	C_{22} (GPa)	C_{23} (GPa)	C_{33} (GPa)	C_{16} (GPa)	C_{26} (GPa)	C_{36} (GPa)	C_{44} (GPa)	C_{55} (GPa)	C_{66} (GPa)	C_{45} (GPa)	K_{Hill} (GPa)	G_{Hill} (GPa)
0	3.338	300.9	66.8	66.5	311.0	53.3	364.1	-25.8	54.4	13.6	108.8	102.5	128.4	42.1	148.7	112.7
10	3.547	391.1	108.0	88.8	384.0	83.0	428.1	-10.6	60.2	20.6	131.8	120.4	167.3	51.0	194.0	136.9
20	3.720	468.1	146.6	112.3	454.6	115.8	488.5	-0.3	67.0	26.3	148.6	134.4	201.6	59.9	237.6	155.5
25	3.797	520.9	172.9	130.5	504.1	137.0	517.9	9.2	72.3	27.4	155.5	140.3	217.6	64.4	266.7	164.5
30	3.865	573.3	198.2	149.4	614.6	177.2	553.4	17.9	91.8	34.5	161.1	145.2	238.4	68.8	304.4	175.8
40	3.986	641.1	238.6	176.2	665.2	207.7	603.8	28.8	93.9	38.6	169.4	153.6	262.1	76.5	344.5	186.2
50	4.098	695.3	269.0	200.1	712.0	238.1	651.6	32.5	96.5	42.1	176.4	161.3	284.4	83.5	379.0	195.2
60	4.202	749.0	303.8	225.3	758.4	268.5	697.7	38.9	98.2	45.0	182.6	168.1	307.4	90.0	415.0	203.4
70	4.300	800.8	338.9	250.4	803.3	297.8	742.2	45.1	100.8	47.7	187.2	174.3	328.3	96.4	450.3	210.2
80	4.393	850.2	375.1	276.2	847.2	326.7	785.8	52.1	103.3	50.2	191.2	180.0	348.4	102.4	485.7	216.2
90	4.481	898.8	408.2	301.5	890.3	355.3	828.6	57.0	105.6	52.3	194.3	185.3	367.9	108.4	519.6	221.6
100	4.565	946.1	440.9	326.6	932.1	383.2	870.2	61.4	107.8	54.2	196.7	190.2	386.9	114.1	552.9	226.3

Table 2. Elastic constants (C_{ij}), bulk (K) and shear (G) moduli of phase H (model-1) as a function of pressure.

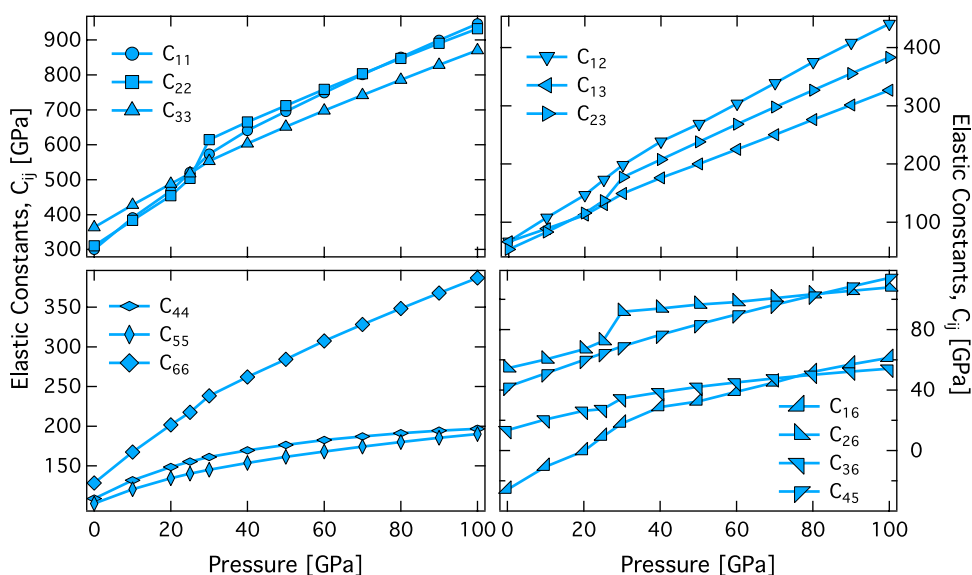


Figure 3. Elastic constants as a function of pressure. Plot shows the full elastic constant tensor for phase H with ordered Mg and Si atoms (model-1) as a function of pressure, upper left panel shows the principle elastic constants- C_{11} , C_{22} , and C_{33} ; upper right panel shows the off diagonal elastic constants- C_{12} , C_{13} , and C_{23} ; lower left panel shows the shear elastic constants- C_{44} , C_{55} , and C_{66} ; and the lower right panel shows the off diagonal elastic constants- C_{16} , C_{26} , C_{36} , and C_{45} . The discontinuous behavior of C_{11} , C_{22} , C_{23} , C_{16} , C_{26} , C_{66} is related to the hydrogen bond symmetrization at 30 GPa.

The bulk (K), shear (G) moduli, primary (V_p), and shear (V_s) velocities for phase H increase upon compression (Fig. 4). The bulk sound velocity (i.e., $V_\phi = (K/\rho)^{0.5}$) is in very good agreement with the recent study on shock wave experimental studies on DHMS phases²⁶ (Supplementary Fig. 1). The discontinuous behavior of K at pressures of ~20–30 GPa is related to the anomalous increase of the principal elastic constants, C_{11} and C_{22} , which is in turn related to the hydrogen bond symmetrization. The effect of Mg-Si order disorder do not show appreciable changes in the bulk and shear moduli throughout the range of pressures explored in this study (Fig. 4). Since phase H and δ -AlOOH are isostructural at conditions relevant to the lower mantle, these two phases could show appreciable solid solution through $\text{Mg} + \text{Si} = 2\text{Al}$ substitutions. This has been observed in recent experimental studies^{18,27}. We notice that in comparison to the aluminous end member δ -AlOOH phase, the primary (V_p), and shear (V_s) velocities are 3% and 4% slower for phase H (Fig. 4), respectively. However, the primary (V_p) sound velocity for the

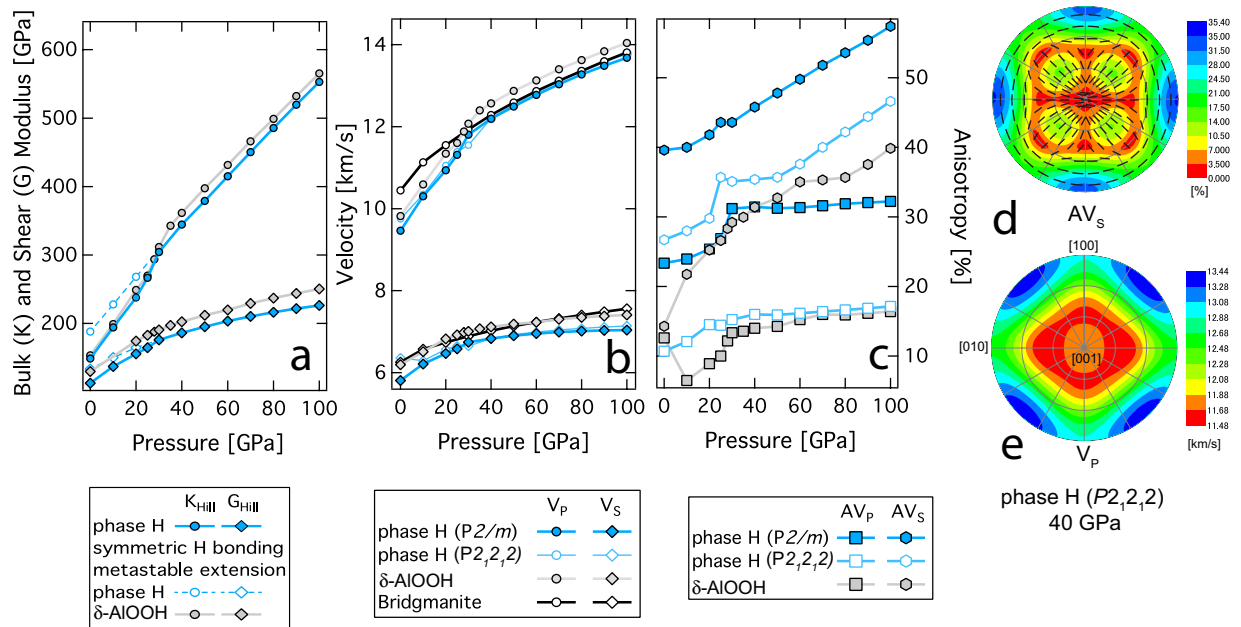


Figure 4. Pressure dependence of elasticity and anisotropy. (a) Plot of bulk and shear moduli as a function of pressure, (b) plot of primary (V_P) and shear (V_S) velocity as a function of pressure, (c) plot of shear wave polarization anisotropy (AV_S) and primary wave azimuthal anisotropy (AV_P) as a function of pressure. Stereographic projection for (d) AV_S and (e) V_P for phase H (model-2) at 40 GPa, clearly indicates orthorhombic symmetry.

volumetrically dominant lower mantle phase, bridgmanite, lies in between that of δ -AIOOH and phase H. The shear sound velocity (V_S) for bridgmanite lies in between that of δ -AIOOH and phase H for a pressure range of 30 to 60 GPa but is greater than both δ -AIOOH and phase H above 60 GPa (Fig. 4). Hence, lower velocities in the deep mantle could be due to a combination of iron enrichment, higher temperatures, and the presence of deeply subducted hydrous phases.

Discussions

The sound wave velocities vary as a function of the propagation direction. The anisotropy in the sound wave velocities could be calculated by solving the Christoffel's equations, $\det|c_{ijkl}n_jn_l - \rho V^2\delta_{ik}| = 0$, where \mathbf{n} , ρ , V , and δ_{ik} are the propagation direction, density, wave velocity, and Kronecker delta, respectively²⁸. The calculated shear wave (V_S) polarization anisotropy (AV_S) is defined as $AV_S = 100 \times (V_{S1} - V_{S2}) / V_S$ and the azimuthal anisotropy for primary wave (AV_P) is defined as $AV_P = 100 \times (V_{Pmax} - V_{Pmin}) / V_P$. The polarization anisotropy AV_S increases with pressure, whereas the azimuthal anisotropy AV_P remains unchanged beyond the hydrogen bond symmetrization pressure ~ 30 GPa. The azimuthal anisotropy AV_P is reduced for the model-2 type disordered structured phase H ($AV_P \sim 18\%$) compared with that of model-1 ($AV_P \sim 32\%$) (Fig. 4, Supplementary Figs 2 and 3), it is still higher than that of bridgmanite ($AV_P \sim 12\%$)²⁹, and post perovskite ($AV_P \sim 15\%$)³⁰ at lower mantle pressures of 100 GPa.

There is no major change of the fast and slow directions of the velocities of phase H between 40 and 100 GPa. The core mantle boundary region is known to be seismically anisotropic and the horizontally polarized shear waves (V_{SH}) propagate faster than vertically polarized ones (V_{SV})³¹. The calculated polarization anisotropy indicates that if the lattice preferred orientation of phase H is developed by aligning the c -axis vertically, the high polarization anisotropy with $V_{SH} > V_{SV}$ could partly explain the observed seismic anisotropy at the bottom of lower mantle.

We also estimated the acoustic impedance contrast ($\Delta I/I$) due to the decomposition of phase D to a mixture of phase H and stishovite at pressure conditions relevant for the upper part of the lower mantle (Fig. 5). Decomposition reaction involving the DHMS phases could partly explain observed seismic impedance contrast at a mid-mantle depths of ~ 1000 km³². If the impedance contrast is indeed partly related to the decomposition of phase D to phase H and stishovite, it would mean that a significant amount of water could be transported into the deep Earth through DHMS phases such as phase D and phase H down to lower mantle depths.

Methods

We used first principles calculations based on the density functional theory to predict the structure, equation of state, and elasticity of phase H. We used generalized gradient approximation (GGA)³³ for

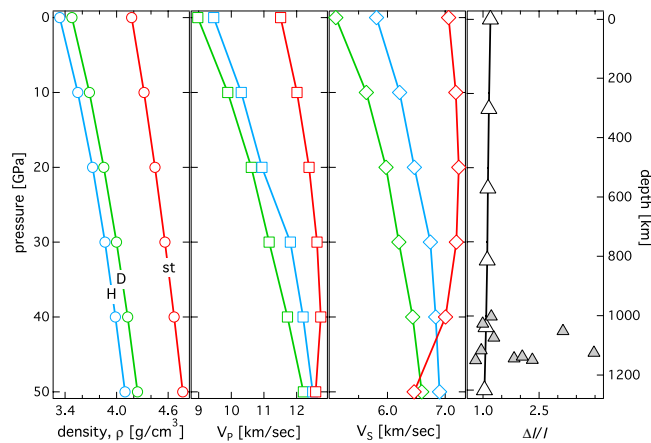


Figure 5. Density, velocity, and impedance contrast. Plot of (a) density, (b) primary wave velocity (V_p), and (c) shear wave velocity (V_s) vs. pressure for phase H (model-1) (H: light blue open symbols), phase D (D: light green open symbol), and stishovite (st: red open symbols). (d) plot of impedance contrast ($\Delta I/I$) (open triangles) defined as the sum of shear velocity contrast and density contrast⁴⁴ across the reaction phase D = phase H + stishovite. Also shown are the depth dependent impedance contrasts from seismological observations (filled grey triangles)³¹.

the description of exchange-correlation functional. Norm-conserving pseudopotentials³⁴ have been employed to describe the ionic core potentials of silicon (Si), oxygen (O), and hydrogen (H), whereas the magnesium (Mg) pseudopotential is generated by the method of U. von Barth and R. Car³⁵. The semi-core p-electrons are not included in the Mg pseudopotential. These potentials were extensively tested in previous studies^{35–37}. GGA has been successfully used in predicting high-pressure behavior of hydrous phases^{38,39} and have been tested experimentally⁴⁰. All structural parameters are fully relaxed at a static 0 K and 0–100 GPa by the damped variable cell shape molecular dynamics method implemented in the Quantum-Espresso codes⁴¹ until residual forces become less than 1.0×10^{-5} Ry/au. The electronic wave function is expanded in plane waves using a kinetic energy cutoff of 80 Ry. The irreducible Brillouin zone of the phase H structure is sampled on a $4 \times 4 \times 6$ Monkhorst-Pack mesh⁴². In addition to the unit cell calculation of phase H, we also conducted the supercells in order to estimate the effect of disordering between Mg and Si onto the cell parameters. K-points in those supercells are sampled on a larger mesh in order to achieve the k-point sampling, which is equivalent to that for the unit cell in reciprocal space. The elastic constants are determined by using the stress-strain relations⁴³. The magnitude of all applied strains was $\pm 1\%$. The linear relation was ensured for this strain range.

Recent first principles simulations reported a fully optimized crystal structure of phase H¹⁷ with a monoclinic symmetry ($\gamma \sim 91^\circ$ at 40 GPa) with space group $P2_1/m$ that was slightly distorted from orthorhombic symmetry. Experimental studies reported that the structure of phase H is orthorhombic with space group $P2_1nm$ ¹⁸ and more recently based on single-crystal X-ray diffraction, a space group of $Pnmm$ ¹⁹ (CaCl_2 type structure) has been proposed. Although, the polyhedral frameworks of crystal structures proposed by all these studies are similar, the Mg and Si were found to be disordered in the octahedral sites¹⁹. In order to mimic the effect of disorder of the Mg and Si in the octahedral sites, we used distinct structural models and evaluate their relative energetics (Fig. 1). Figure 1 shows the calculated model crystal structures. All these models are derivative of the previous first principles simulations with $P2_1/m$ space group symmetry. Model-1 corresponds to the ordered Mg and Si crystal structure (cell size $\mathbf{a} \times \mathbf{b} \times \mathbf{c}$)¹⁷, Model-2 ($\mathbf{a} \times \mathbf{b} \times 2\mathbf{c}$ supercell) where Mg and Si atoms are alternatively arranged along the c -axis resulting in an orthorhombic space group symmetry $P2_12_12$, and Model-3 ($2\mathbf{a} \times 2\mathbf{b} \times \mathbf{c}$ supercell) where Mg and Si atoms are alternatively placed along the \mathbf{a} - and \mathbf{b} - axes with monoclinic space group symmetry $P2_1/m$ (Fig. 1). We have fully optimized the cell parameters of these model structures at 0–100 GPa. We also calculate the full elastic constant tensor for model-1 and model-2 (Supplementary Table 1). In order to compare the elasticity of phase H with that of the major lower mantle phase, we have also calculated the elastic constants of bridgmanite using the same pseudopotentials as those used for the calculation of phase H (Supplementary Fig. 1).

References

- Iwamori, H. Transportation of H_2O and melting in subduction zones. *Earth Planet. Sci. Lett.* **160**, 65–80 (1998).
- Karato, S.-I., Paterson, M. S. & FitzGerald, J. D. Rheology of synthetic olivine aggregates: Influence of grain size and water. *J. Geophys. Res.* **91**(B8), 8151–8176 (1986).
- Mei, S. & Kohlstedt, D. L. Influence of water on plastic deformation of olivine aggregates: 1. Diffusion creep regime. *J. Geophys. Res.* **105**(B9), 21457–21469 (2000).
- Mei, S. & Kohlstedt, D. L. Influence of water on plastic deformation of olivine aggregates: 2. Dislocation creep regime. *J. Geophys. Res.* **105**(B9), 21471–21481 (2000).

5. van Keken, P. E., Hacker, B. R., Syracuse, E. M. & Abers, G. A. Subduction factory: 4. Depth-dependent flux of H₂O from subducting slabs worldwide. *J. Geophys. Res.* **116**, B01401 (2011).
6. Frost, D. J. The stability of hydrous mantle phases. *Rev. Min. Geochem.* **62**, 243–271 (2006).
7. Kawamoto, T. Hydrous phases and water transport in the subducting slab. *Rev. Min. Geochem.* **62**, 273–289 (2006).
8. Angel, R. J., Frost, D. J., Ross, N. L. & Hemley, R. Stabilities and equations of state of dense hydrous magnesium silicates. *Phys. Earth Planet. Int.* **127**, 181–196 (2001).
9. Ranero, C. R., Phipps-Morgan, J., Mcintosh, K. & Reichert, C. Bending-related faulting and mantle serpentinization at the middle America trench. *Nature* **425**, 367–373 (2003).
10. Faccenda, M., Burlini, L., Gerya, T. V. & Mainprice, D. Fault-induced seismic anisotropy by hydration in subducting oceanic plates. *Nature* **455**, 1097–1100 (2008).
11. Schmidt, M. W. & Poli, S. Experimentally based water budgets for dehydrating slabs and consequences for arc magma generation. *Earth Planet. Sci. Lett.* **163**, 361–379 (1998).
12. Ohtani, E., Toma, M., Litasov, K., Kubo, T. & Suzuki, A. Stability of dense hydrous magnesium silicate phases and water storage capacity in the transition zone and lower mantle. *Phys. Earth Planet. Int.* **124**, 105–117 (2001).
13. Liu, L. Effects of H₂O on the phase behaviour of the forsterite-enstatite system at high pressures and temperatures and implications for the Earth. *Phys. Earth Planet. Int.* **49**, 142–167 (1987).
14. Frost, D. J. & Fei, Y. Stability of phase D at high pressure and high temperature. *J. Geophys. Res.* **103**, 7463–7474 (1998).
15. Shieh, S. R., Mao, H.-K., Hemley, R. J. & Ming, L. C. Decomposition of phase D in the lower mantle and the fate of dense hydrous silicates in subducting slabs. *Earth Planet. Sci. Lett.* **159**, 13–23 (1998).
16. Shieh, S. R., Mao, H.-K., Hemley, R. J. & Ming, L. C. *In situ* X-ray diffraction studies of dense hydrous magnesium silicates at mantle conditions. *Earth Planet. Sci. Lett.* **177**, 69–80 (2000).
17. Tsuchiya, J. First principles prediction of a new high-pressure phase of dense hydrous magnesium silicates in the lower mantle. *Geophys. Res. Lett.* **40**, 4570–4573 (2013).
18. Nishi, M. *et al.* Stability of hydrous silicate at high pressures and water transport to the deep lower mantle. *Nature Geosci.* **7**, 224–227 (2014).
19. Bindi, L., Nishi, M., Tsuchiya, J. & Irifune, T. Crystal chemistry of dense hydrous magnesium silicates: the structure of phase H, MgSiH₂O₄, synthesized at 45 GPa and 1000 °C. *Am. Mineral.* **99**, 1802–1805 (2014).
20. Murnaghan, F. D. The compressibility of media under extreme pressures. *Proc. Natl. Acad. Sci. USA* **30**(9), 244–247 (1944).
21. Tsuchiya, J. & Tsuchiya, T. Elastic properties of δ-AIOOH under pressure: First principles investigation. *Phys. Earth Planet. Int.* **174**, 122–127 (2009).
22. Panero, W. R. & Stixrude, L. Hydrogen incorporation in stishovite at high pressure and symmetric hydrogen bonding in δ-AIOOH. *Earth Planet. Sci. Lett.* **221**, 421–431 (2004).
23. Sano-Furukawa, A., Komatsu, K., Vanpeteghem, C. B. & Ohtani, E. Neutron diffraction study of δ-AIOOH at high pressure and its implication for symmetrization of the hydrogen bond. *Am. Mineral.* **93**, 1558–1567 (2008).
24. Sano-Furukawa, A. *et al.* Change in compressibility of δ-AIOOH and δ-AIOOD at high pressure: A study of isotope effect and hydrogen-bond symmetrization. *Am. Mineral.* **94**, 1255–1261 (2009).
25. Benoit, M., Marx, D. & Parrinello, M. Tunnelling and zero-point motion in high-pressure ice. *Nature* **392**, 258–261 (1998).
26. Zhang, Y., Sekine, T. & He, H. A new interpretation of decomposition products of serpentine under shock compression. *Am. Mineral.* **99**, 2374–2377 (2014).
27. Ohira, I. *et al.* Stability of a hydrous δ-phase, AIOOH-MgSiO₂(OH)₂, and a mechanism for water transport into the base of lower mantle. *Earth Planet. Sci. Lett.* **401**, 12–17 (2014).
28. Musgrave, M. J. P. *Crystal Acoustics* (Holden-Day, San Francisco, 1970).
29. Wentzcovitch, R. M., Karki, B. B., Karato, S. & Da Silva, C. R. S. High pressure elastic anisotropy of MgSiO₃ perovskite and geophysical implications. *Earth Planet. Sci. Lett.* **164**, 371–378 (1998).
30. Tsuchiya, T., Tsuchiya, J., Umemoto, K. & Wentzcovitch, R. M. Elasticity of post-perovskite MgSiO₃. *Geophys. Res. Lett.* **31**, L14603 (2004).
31. Lay, T., Williams, Q. & Garnero, E. J. The core-mantle boundary layer and deep earth dynamics. *Nature* **392**, 461–468 (1998).
32. Courtier, A. M. & Revenaugh, J. Slabs and shear wave reflectors in the mid mantle. *J. Geophys. Res.* **113**, B08312 (2008).
33. Perdew, J. P., Burke, K. & Ernzerhof, M. Generalized Gradient Approximation made simple. *Phys. Rev. Lett.* **77**, 3865–3868 (1996).
34. Troullier, N. & Martins, J. L. Efficient pseudopotentials for plane-wave calculations. *Phys. Rev. B* **43**, 1993–2006 (1991).
35. Karki, B. B., Wentzcovitch, R. M., de Gironcoli, S. & Baroni, S. Ab initio lattice dynamics of MgSiO₃ perovskite at high pressure. *Phys. Rev. B* **62**, 14750 (2000).
36. Tsuchiya, J. & Tsuchiya, T. First principles investigation of the structural and elastic properties of hydrous wadsleyite under pressure. *J. Geophys. Res.* **114**, B02206 (2009).
37. Tsuchiya, J. & Tsuchiya, T. Elastic properties of phase D (MgSi₂O₆H₂) under pressure: Ab initio investigation. *Phys. Earth Planet. Int.* **170**, 215–220 (2008).
38. Jahn, S. *et al.* Pressure-induced hydrogen bond symmetrization in guyanite, β-CrOOH: evidence from spectroscopy and ab initio simulations. *Eur. J. Mineral.* **24**, 839–850 (2012).
39. Mainprice, D., LePage, Y., Rodgers, J. & Jouanna, P. Predicted elastic properties of hydrous D phase at mantle pressures: Implications for the seismic anisotropy of subducted slabs near 670 km discontinuity and in the lower mantle. *Earth Planet. Sci. Lett.* **259**, 283–296 (2007).
40. Rosa, A. D. *et al.* Shear wave anisotropy in textured phase D and constraints on deep water recycling in subduction zones. *Earth Planet. Sci. Lett.* **377–378**, 13–22 (2013).
41. Giannozzi, P. *et al.* QUANTUM ESPRESSO: A modular and open-source software project for quantum simulations of materials. *J. Phys. Condens. Matter.* **21**, 395502 (2009).
42. Monkhorst, H. J. & Pack, J. D. Special points for Brillouin-zone integrations. *Phys. Rev. B* **13**, 5188–5192 (1976).
43. Karki, B. B., Stixrude, L. & Wentzcovitch, R. M. High-pressure elastic properties of major materials of earth's mantle from first principles. *Rev. Geophys.* **39**, 507–534 (2001).
44. Stixrude, L. Properties of rocks and minerals- Seismic properties of rocks and minerals, and the structure of the Earth, Treatise on Geophysics. *Mineral. Phys.* **2**, 7–32 (2007).

Acknowledgements

JT thanks Grants-In-Aid for Scientific Research, KAKENHI (Nos. 26400516, 26287137, 15H05834) from the Japan Society for the Promotion of Science. MM is currently supported by the US National Science Foundation grant (EAR-1250477, EAR-1520726).

Author Contributions

J.T. and M.M. jointly analyzed the results and wrote the article.

Additional Information

Supplementary information accompanies this paper at <http://www.nature.com/srep>

Competing financial interests: The authors declare no competing financial interests.

How to cite this article: Tsuchiya, J. and Mookherjee, M. Crystal structure, equation of state, and elasticity of phase H (MgSiO_4H_2) at Earth's lower mantle pressures. *Sci. Rep.* **5**, 15534; doi: 10.1038/srep15534 (2015).



This work is licensed under a Creative Commons Attribution 4.0 International License. The images or other third party material in this article are included in the article's Creative Commons license, unless indicated otherwise in the credit line; if the material is not included under the Creative Commons license, users will need to obtain permission from the license holder to reproduce the material. To view a copy of this license, visit <http://creativecommons.org/licenses/by/4.0/>